International Journal of Pharmaceutics 662 (2024) 124516

Contents lists available at ScienceDirect

International Journal of Pharmaceutics

journal homepage: www.elsevier.com/locate/ijpharm

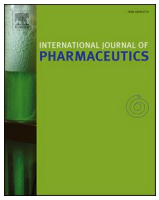

Preclinical characterization of endotoxin-induced uveitis models using OCT, PET/CT and proteomics

Andrea Cuartero-Martínez [a,b,1], Xurxo García-Otero [b,c,d,1], Jessica Codesido [a,b,c], Noemí Gómez-Lado [c,d], Jesús Mateos [a], Susana B. Bravo [e], Carmen Antía Rodríguez-Fernández [a,f], Miguel González-Barcia [a], Pablo Aguiar [c,d], Marcos Ortega-Hortas [g,*], Francisco J. Otero-Espinar [b,h,i,**], Anxo Fernández-Ferreiro [a,***]

[a] FarmaChusLab Group, Health Research Institute of Santiago de Compostela (FIDIS), 15706 Santiago de Compostela, Spain
[b] Department of Pharmacology, Pharmacy and Pharmaceutical Technology, Faculty of Pharmacy, University of Santiago de Compostela (USC), 15782 Santiago de Compostela, Spain
[c] Molecular Imaging Biomarkers and Theragnosis Lab, Center for Research in Molecular Medicine and Chronic Diseases (CiMUS), University of Santiago de Compostela (USC), Santiago de Compostela, Spain
[d] Nuclear Medicine Service and Molecular Imaging Group, Health Research Institute of Santiago de Compostela (FIDIS), 15706 Santiago de Compostela, Spain
[e] Proteomic Unit, Health Research Institute of Santiago de Compostela (IDIS), 1570f Santiago de Compostela, Spain
[f] Ophthalmology Department, Vall d'Hebron University Hospital, 08035 Barcelona, Spain
[g] VARPA Group, INIBIC. Research Center CITIC, University of A Coruña, 15071 A Coruña, Spain
[h] Paraquasil Group, Health Research Institute of Santiago de Compostela (IDIS), 15706 Santiago de Compostela, Spain
[i] Institute of Materials (iMATUS), University of Santiago de Compostela (USC), 15782 Santiago de Compostela, Spain

ARTICLE INFO

Keywords:
Model characterization
Endotoxin-induced uveitis models
Ocular inflammatory diseases
OCT imaging
Proteomics
PET/CT imaging

ABSTRACT

Uveitis is a group of inflammatory ocular pathologies. Endotoxin-Induced Uveitis (EIU) model represent a well-known model induced by administration of Lipopolysaccharide (LPS). The aim is to characterize two models of EIU through two routes of administration with novel noninvasive imaging techniques. 29 rats underwent Intraocular Pressure (IOP) measurements, Optical Coherence Tomography (OCT), proteomic analysis, and Positron Emission Tomography and Computed Tomography (PET/CT). Groups included healthy controls (C), BSS administered controls (Ci), systemically induced EIU with LPS (LPSs), and intravitreally induced EIU with LPS (LPSi) for IOP, OCT, and proteomic studies. For ^{18}F-FDG PET/CT study, animals were divided into FDG-C, FDG-LPSs and FDG-LPSi groups and scanned using a preclinical PET/CT system. LPSi animals exhibited higher IOP post-induction compared to C and LPSs groups. LPSi showed increased cellular infiltrate, fibrotic membranes, and iris inflammation. Proinflammatory proteins were more expressed in EIU models, especially LPSi. PET/CT indicated higher eye uptake in induced models compared to FDG-C. FDG-LPSi showed higher eye uptake than FDG-LPSs but systemic uptake was higher in FDG-LPSs due to generalized inflammation. OCT is valuable for anterior segment assessment in experimental models. ^{18}F-FDG PET/CT shows promise as a noninvasive biomarker for ocular inflammatory diseases. Intravitreal induction leads to higher ocular inflammation. These findings offer insights for future inflammatory disease research and drug studies.

* Corresponding authors at: VARPA Group, INIBIC. Research Center CITIC, University of A Coruña, 15071 A Coruña, Spain.
** Corresponding authors at: Department of Pharmacology, Pharmacy and Pharmaceutical Technology, Faculty of Pharmacy, University of Santiago de Compostela (USC), 15782 Santiago de Compostela, Spain.
*** Corresponding authors at: FarmaChusLab Group, Health Research Institute of Santiago de Compostela (FIDIS), 15706 Santiago de Compostela, Spain.
E-mail addresses: andrea.cuartero@rai.usc.es (A. Cuartero-Martínez), xurxo.garcia.otero@usc.es (X. García-Otero), jessicafraga.codesido@usc.es (J. Codesido), noemi.gomez@usc.es (N. Gómez-Lado), Jesus.Mateos.Martin@sergas.es (J. Mateos), Susana.Belen.Bravo.Lopez@sergas.es (S.B. Bravo), miguel.gonzalez.barcia@sergas.es (M. González-Barcia), pablo.aguiar.fernandez@gmail.com (P. Aguiar), m.ortega@udc.es (M. Ortega-Hortas), francisco.otero@usc.es (F.J. Otero-Espinar), anxordes@gmail.com (A. Fernández-Ferreiro).
[1] These authors contributed equally to this work.

https://doi.org/10.1016/j.ijpharm.2024.124516
Received 16 May 2024; Received in revised form 23 July 2024; Accepted 24 July 2024
Available online 25 July 2024

1. Introduction

Uveitis includes a group of eye diseases of different etiologies that involve inflammation of the uvea (iris, ciliary body and choroid) (Chang et al., 2021; Jabs et al., 2005). In developed countries, the incidence of uveitis is estimated to range from 17 to 52 per 100,000 habitants per year (Tsirouki et al., 2018). Clinical evaluation of the disease includes a visual acuity test, an ocular surface and anterior chamber examination with a slit lamp a vitreous and retina examination with an ophthalmoscope (Wang et al., 2021) and currently, Optical Coherence Tomography (OCT) (Invernizzi et al., 2019; Qu et al., 2022). In addition, Intraocular Pressure (IOP) should be measured in the management of uveitis to prevent potential damage to the optic nerve (Chang et al., 2021).

OCT is a noninvasive imaging technique that provides *in vivo* tissue images with micrometer resolution based on low coherence interferometry principle (Aumann et al., 2019), generating images due to the interaction of the light beam with the different ocular structures. Ocular structures absorb light depending on their molecular structure (Invernizzi et al., 2019; Venkateswaran et al., 2018). OCT supply detailed structural information about anterior and posterior segment of the eye being a helpful instrument to find the main complications of uveitis in an easy and noninvasive way (Invernizzi et al., 2019; Reddy et al., 2014). Anterior OCT, also known as an Anterior Segment Optical Coherence Tomography (AS-OCT) provides a detailed imaging of the structures in the front portion of the eye, allowing the evaluation of cellular infiltrate, fibrotic membranes, and changes in iris morphology, among others (Agarwal and Invernizzi, 2022; Pichi et al., 2022). Initially, OCT was developed for clinical practice, but nowadays, its use in preclinical studies has been further investigated due to its reproducibility. In preclinical studies of uveitis, OCT has been used to detect the main clinical signs of the disease (Choi et al., 2018; Fan et al., 2021; Gadjanski et al., 2011; Pepple et al., 2016).

According to the 3Rs principles in animal experimentation (William and Burch, 1960) alternatives are currently being sought for the diagnosis, characterization and follow-up of this pathology. Positron Emission Tomography (PET) is a noninvasive medical imaging technique that allows the use of radioactive-labeled molecules known as radiotracers to characterize the biological function of the imaged tissues (Crișan et al., 2022; Rong et al., 2023). PET has a wide range of uses, from disease characterization to antibody biodistribution studies and pharmacokinetic studies. With this technology (Crișan et al., 2022), the physiological information obtained by PET can be combined with the anatomical information provided by Computed Tomography (CT) to obtain PET/CT images. The use of PET/CT with the radiotracer ^{18}F-Fluoro-2-Deoxy-2-D-Glucose (^{18}F-FDG), a glucose metabolism marker used to identify areas where there is abnormally high glucose metabolism (Glaudemans et al., 2013), has been shown to be highly sensitive in the identification of inflammatory involvement.

Uveitis can provoke a breakdown of the blood-retinal barrier and changes in ocular physiology (Bansal and Gupta, 2020; Chang et al., 2021; Girol et al., 2013), so different protein biomarkers have been identified in clinical and preclinical models of uveitis disease (Imai et al., 2010; Pepple et al., 2015; Rao et al., 2008; Wang et al., 2015; Zhang et al., 2022). High-resolution quantitative proteomics is a tool that allows the identification of modulated proteins in biological processes such as diseases and aging, as well as the investigation of changes in this modulation due to pharmacological treatments or gene therapy (Mateos et al., 2014; Sivanich et al., 2022).

In the study of uveitis, numerous preclinical models have been performed to investigate the pathophysiology of the disease and evaluate the potential of different pathways and new treatments. One of this widely accepted animal models is the Endotoxin-Induced Uveitis rat model (EIU) by Lipopolysaccharide (LPS) administration (Yadav and Ramana, 2019). Its administration contributes to the activation of the inflammatory cascade, favoring the rupture of the blood-retinal barrier by acting on the Toll-Like Receptor 4-dependent pathway (TLR4) (Mérida et al., 2015). Few works have studied the phenotypic differences in uveitis disease based on the type of endotoxin administration (Rosenbaum et al., 2011). Comparison of the models according to type of administration on ocular inflammation was performed through quantification and analysis of *ex vivo* studies but in our knowledge this comparison does not yet exist in *in vivo* and noninvasive studies.

Therefore, the aim of the present work is to characterize two models of EIU through two routes of administration, systemic and intravitreal, with novel noninvasive imaging techniques (OCT and PET/CT) and to make a comparison between them with an ocular proteomic study of the evaluated models.

2. Materials and methods

2.1. Materials

Escherichia coli LPS endotoxin was obtained from Sigma-Aldrich (Sant Louis, USA). Balance Salt Solution (BSS) was adquired from Alcon Healthcare (Texas, USA). Isoflurane was purchased from Baxter® (Illinois, USA), Ketamine was obtained from Pfizer (Ketolar, Madrid, USA) and Xilacine was adquired from Fatro Iberica (Nerfasin, Barcelona, ES). Colirofta® Ciclopléjico (10 mg/mL cyclopentolate hydrochloride), Colircusi® Anestesico doble (1 mg/mL tetracaine hydrochloride, 4 mg/mL oxybuprocaine Hydrochloride) and ACUOLENS® artificial tear (3 mg/mL Hypromellose and 5.5 mg/mL sodium chloride) were obtained from Alcon Healthcare (Texas, USA). For the proteomic analysis, Trizol Reagent was obtained from Merck (Darmstadt, GE) and Urea 8 M, TRIS-Hydrocloric acid (TRIS-HCl) and Sodium Dodecil Sulfate 1 % (SDS) were purchase from Sigma Aldrich (San Louis, USA).

2.2. Animals

Twenty-nine male Sprague Dawley rats supplied by the Center for Experimental Biomedicine of Galicia of the University of Santiago de Compostela (CEBEGA, Santiago de Compostela, Spain) were used. The mean weight of the animals was 262 ± 14 g, and age was six weeks. The animals were maintained on food and water *ad libitum* in SPF conditions with controlled humidity (41 ± 1.8 %) and temperature (23.5 ± 0.5 °C) with 12-hour regulated day-night cycles. Animals were treated according to the ARVO statement for the use of animals in ophthalmic and vision research, as well as the approved guidelines for laboratory animals (ARVO, 2021; National Research Council (US), 2011). The study protocols were approved by the Committee for Ethical Research of the Health Research Institute of Santiago de Compostela (IDIS) (15012/2021/001) and followed the Spanish and European Union (EU) rules (86/609/CEE, 2003/ 65/ CE, 2010/63/EU, RD 1201/2005, and RD53/2013).

Twenty rats were used for IOP measurements, OCT imaging studies, and proteomics in order to determine the degree of ocular inflammation. For IOP measurements and OCT studies, animals were evaluated in 4 homogeneous groups: a control group of healthy rats (C, n = 5, 10 eyes), another control group in which BSS was injected intravitreally (Ci, n = 5, 10 eyes), a uveitis group of systemically endotoxin-induced uveitis (LPSs, n = 5, 10 eyes), and a second uveitis group of intravitreally endotoxin-induced uveitis (LPSi, n = 5, 10 eyes). For the proteomic study, 5 eyes of each group were used (one eye per rat).

After studying the possible existence of inflammation associated with the LPS administration, the remaining nine rats were used in the characterization of both uveitis models by preclinical FDG PET/CT. This study provides information about whole-body inflammation as well as that produced in the eye. Animals were divided into three groups: control group of healthy animals (FDG-C, n = 3, 6 eyes), uveitis group induced by systemic route (FDG-LPSs, n = 3, 6 eyes), and uveitis group induced by intravitreal injection (FDG-LPSi, n = 3, 6 eyes). At the end of the *in vivo* experiments, the animals were sacrificed by carbon dioxide inhalation. The experimental design of the study is shown in Fig. 1.

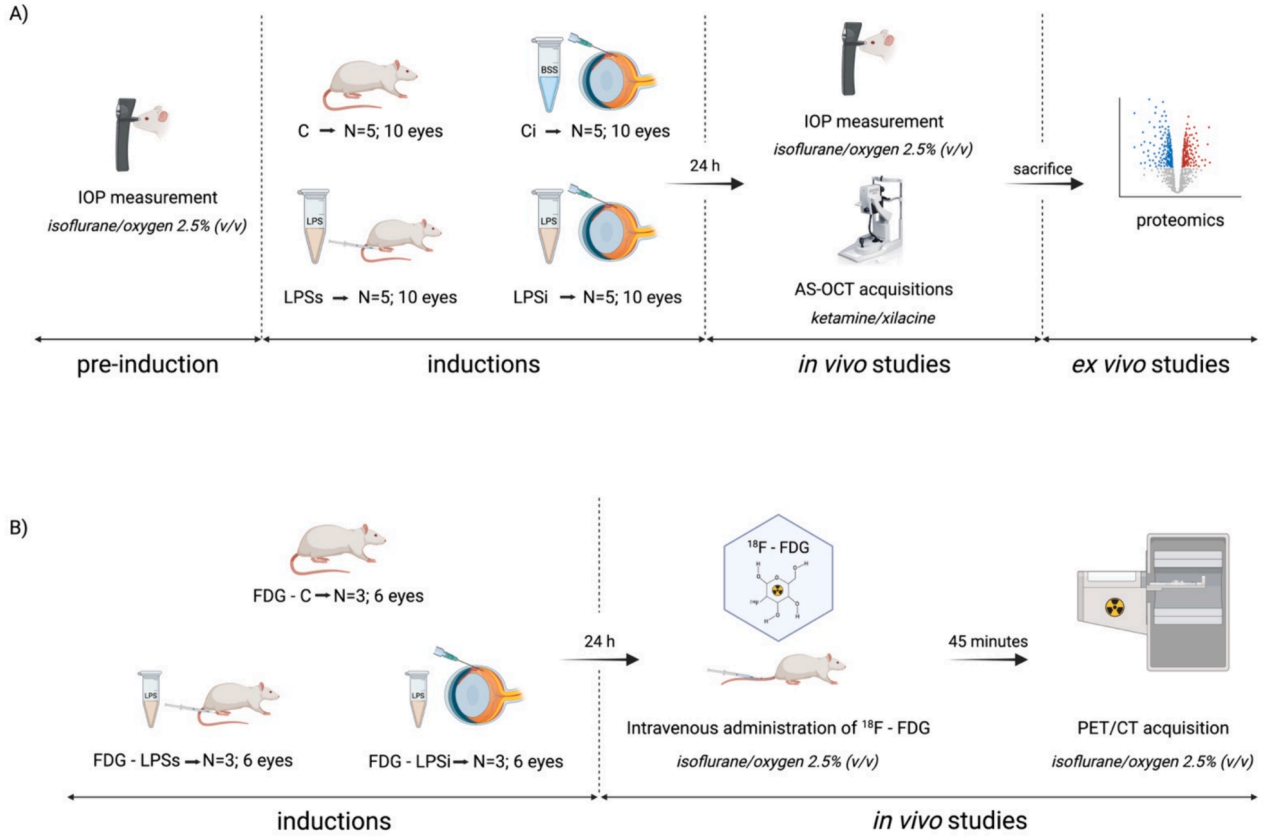

Fig. 1. Experimental diagram of the different studies: A) IOP measurements, AS-OCT imaging studies and proteomics for the four experimental groups (control (C), intravitreal control (Ci), systemically induced uveitis (LPSs) and intravitreally induced uveitis (LPSi)). B) PET imaging studies. Control group (C) and EIU model inductions of the LPSs and LPSi groups, intravenous administration of ^{18}F-FDG and PET/CT acquisitions. Created with BioRen-der.com.

2.3. In vivo Endotoxin-Induced uveitis model (EIU Model)

In this study, two types of EIU induction were evaluated: systemic and intravitreal route. To the systemic route, the same protocol used in previous articles was carried out injecting 1 mg/Kg of *Escherichia coli* LPS endotoxin diluted in 0.1 mL balance salt solution (BSS™, Alcon Healthcare, Texas, USA) into the rat's right paw (da Silva et al., 2011; García-Otero et al., 2022, 2021; Girol et al., 2013). For the induction of the intravitreal model, 2 μL of LPS dissolved in PBS at a concentration of 0.125 μg/mL (250 ng of LPS) were injected into the vitreous chamber via *pars plana* using a Hamilton syringe with a 35G needle according to García-Otero *et al.* (García-Otero et al., 2022, 2021).

Before uveitis induction, animals were anesthetized in a gas chamber with 3 % (v/v) isoflurane/oxygen (Baxter®, Deerfield, Illinois, USA). During inductions, animals were anesthetized in a platform with a face mask with 2–2.5 % of isoflurane/oxygen. Prior to the intravitreal injection, animals were instilled in both eyes with a topical anesthetic eye drop (1 mg/mL tetracaine hydrochloride, 4 mg/mL oxybuprocaine Hydrochloride; Colircusí® Anestésico doble, Alcon Healthcare, Texas, USA) followed by a mydriatic eye drop (10 mg/mL cyclopentolate hydrochloride; Colirofta® Ciclopléjico, Alcon Healthcare, Texas, USA). For Ci group, 2 μL of BSS was administered intravitreally in each eye with a surgical lamp and using a Hamilton syringe with a 35G needle (Fernández-Ferreiro et al., 2017; Luaces-Rodríguez et al., 2020). The induction models and the intravitreal injection of BSS were performed 24 h before all the studies, based on the maximum peak of inflammation reached at this time according to scientific evidence provided by other authors (Bermudez et al., 2016). The integrity of the eye, including lens damage and hemorrhage after intravitreal injection was evaluated by surgical lamp before imaging procedures.

2.4. Intraocular pressure measurements (IOP)

All animals included in the IOP study were evaluated at two different time points (before induction or injection and 24 h after induction or injection). To ensure ocular integrity, the IOP measurement was prior to pupil dilation and AS-OCT acquisition. For this purpose, the animals were previously anesthetized with 3.0 % isoflurane/oxygen and the measurements were carried out on a flat platform in prone position. The instrument used for IOP measurement was a rodent rebound tonometer previously calibrated for rat (iCare TonoLab, Icare, Finland, Oy). A triplicate measurement was carried out 6 times each.

2.5. OCT acquisition and image analysis

Before OCT acquisition, animals were anesthetized by intraperitoneal injection of a mixture of 75 mg/kg of Ketamine (Ketolar 50 mg/mL, Pfizer, Madrid, ES), and 10 mg/kg of Xilacine (Nerfasin 20 mg/mL, Fatro Iberica, Barcelona, ES). Subsequently, a mydriatic eye drop (10 mg/mL cyclopentolate hydrochloride; Colirofta® Ciclopléjico, Alcon Healthcare, Texas, USA) and one drop of artificial tear (3 mg/mL Hypromellose and 5.5 mg/mL sodium chloride; ACUOLENS®, Alcon Healthcare, Texas, USA) were instilled to dilate the pupil and to avoid as much as possible the dryness of the ocular surface and spontaneous cataracts due to the anesthesia.

After the animals were checked to ensure that it was fully anesthetized, animals were moved to the Spectralis OCT system to carry out a structural examination of the anterior chamber and the retina. Throughout the procedure, animals were kept on a flat platform with a heating blanket to avoid possible hypothermia caused by prolonged anesthetic exposure (Arras et al., 2001). Each animal was place in prone position with the eye perpendicular to the instrument lens to ensure

maximum axial image quality.

A Spectralis® Spectral-Domain OCT (SD-OCT) was used for this study (SPECTRALIS® OCT, Heidelberg Engineering, Germany). Modifications to the clinical software, such as manual adaptation of the axial reference point, were introduced to evaluate the ocular structures of the rodents. Spectralis consist of a Confocal Laser Scanner (cSLO) connected to a spectral-domain OCT to provide an Infrared (IR) imaging and OCT scanning. The wavelength of IR laser and OCT-cSLO used was 815 and 880 nm, respectively, with an A-scan rate of 40 kHz/85 kHz in retinal imaging. A+21 D lens was used in the mount for the structural study of the anterior chamber. In addition, if the evolution of the disease allowed it, a subsequent retinal examination was performed using a volumetric study centered on the optic nerve.

For the three-dimensional examination of the anterior segment, the entire OCT image was examined using a pattern of 81B-scans with a size pattern of 8 x 5.6 mm (axial x lateral) and the distance between B-scans was 69 μm. For each eye, a region of interest was chosen consisting of the one with the maximum number of B-scans, without those that did not provide complete information about the structure of the anterior chamber.

Ocular signs were evaluated in three B-scans of five regions for each animal (crossing the corneal center, middle superior, superior, middle inferior and inferior). Clinical signs were compared with the anterior chamber image of heathy control animals. Changes in the anterior chamber structure consisted of clear signs of inflammation characteristic of uveitis disease, such as cellular infiltrate, presence of fibrotic membrane and inflammation of the iris and ciliary body. The presence of turbidity and cellular infiltrate in the vitreous chamber was assessed in cases where posterior segment examination could be performed.

2.6. Protein preparation for proteomics analysis

Whole eyes were homogenized in Trizol Reagent (Merck, Darmstadt, Germany) following manufacturer instructions and the protein extract was mixed at a 1:1 ratio in 8 M UREA in 1 M TRIS – HCl, pH 8.0 and SDS 1 % in PBS. Total protein was quantified by Bicinchoninic Acid assay (BCA, Thermo Fisher Scientific, Waltham, MA, USA). Equal amounts of proteins were processed as previously described López-López *et al.* (López-López et al., 2021). Briefly, samples were loaded on a 10 % SDS-PAGE gel. The run was stopped as soon as the front had penetrated 3 mm into the resolving gel. The protein band was detected by Sypro® Ruby Protein Gel Stain (Lonza, Visp, Switzerland), excised, and processed for in-gel, manual tryptic digestion as described Shevchenko *et al.* (Shevchenko et al., 1996). Peptides were extracted by carrying out three 20-min incubations in 40 μL of 60 % Acetonitrile (ACN) dissolved in 0.5 % Formic acid (HCOOH). The resulting peptide extracts were pooled, concentrated in a centrifugal evaporator (Genevac miVac, SP Genevac™ SCIENTIFIC, Warminster, PA, USA), and stored at − 20 °C, until Mass Spectrophotometry (MS) assay was performed.

2.7. Spectral library generation by Data-Dependent acquisition

In order to build the MS/MS spectral libraries, the peptide solutions were analyzed by a shotgun Data-Dependent Acquisition (DDA) approach using micro-Liquid Chromatography-MS/MS (micro-LC-MS/MS). To obtain a good representation of the peptides and proteins present in all samples, pooled vials of samples from each group were prepared using an equal mixture of the original samples. One 4 μL of each pool was separated into a micro-LC system Ekspert nLC425 (Eksigen, Dublin, CA, USA) using an YCM-TriartC18 column (150 μm × 0.3 mm, 12 nm, s-3 μm) (YMC CO, Japan) at a flow rate of 5 μL/min. Water and ACN, both containing 0.1 % HCOOH, were used as solvents A and B, respectively. The gradient run consisted of 5 % to 95 % B for 30 min, 5 min at 90 % B and finally 5 min at 5 % B for column equilibration, for a total run time of 40 min. As the peptides eluted, they were directly injected into a hybrid quadrupole-TOF MS Triple TOF 6600 (Sciex, Redwood City, CA, USA) operated with a data-dependent acquisition system in positive ion mode. A Micro source (Sciex, Redwood City, CA, USA) was used for the interface between microLC and MS, with an application of 2600 V voltage. The acquisition mode consisted of a 250 ms survey MS scan from 400 to 1250 *m/z* followed by an MS/MS scan from 100 to 1500 *m/z* (25 ms acquisition time) of the top 65 precursor ions from the survey scan, for a total cycle time of 2.8 s. The fragmented precursors were then added to a dynamic exclusion list for 15 s; any singly charged ions were excluded from the MS/MS analysis.

The peptide and protein identifications were performed using Protein Pilot software (version 5.0.1, Sciex, Redwood City, CA, USA) from Rattus Novergicus Uniprot database (freely available at https://www.uniprot.org/. Data base release 2023_05 that contain 8313 proteins), specifying iodoacetamide as Cys alkylation. The False Discovery Rate (FDR) was set to 1 for both peptides and proteins. Then, the MS/MS spectra of the identified peptides were used to generate the spectral library for SWATH peak extraction using the add-in for PeakView Software (version 2.2, Sciex, Redwood City, CA, USA) MS/MS and ALL with SWATH Acquisition MicroApp (version 2.0, Sciex, Redwood City, CA, USA). Peptides with a confidence score above 99 % (as obtained from Protein Pilot database search were included in the spectral library).

2.8. Relative quantification by SWATH acquisition

Sequential Window Acquisition of all Theoretical Mass Spectra (SWATH – MS) was performed on a TripleTOF® 6600 LC-MS/MS system (Sciex, Redwood City, CA, USA). Samples from tears samples were analyzed using a Data-Independent Acquisition (DIA) method making 3 technical replicates for each sample (12 total samples). Each sample (4 μL) was analyzed using the LC-MS equipment and LC gradient described above for building the spectral library but instead using the SWATH-MS acquisition method. The method consisted of repeating a cycle of 65 TOF MS/MS scans of overlapping sequential precursor isolation windows of variable width (1 *m/z* overlap) covering the 400 to 1250 *m/z* mass range with a previous TOF MS scan (400 to 1500 *m/z*, 50 ms acquisition time) for each cycle. Total cycle time was 6.3 s. For each sample set, the width of the 100 variable window was optimized according to the ion density found in the DDA runs using a SWATH variable window calculator worksheet from Sciex.

2.9. Proteomics data analysis

The targeted data extraction of the fragment ion chromatogram traces from the SWATH runs was performed by PeakView (version 2.2) using the SWATH Acquisition MicroApp (version 2.0). This application processed the data using the spectral library created from the shotgun data. Up to 10 peptides per protein and 7 fragments/transitions per peptide were selected, based on signal intensity; any shared and modified peptides were excluded from the processing. Five-minute windows and 30 ppm widths were used to extract the ion chromatograms; SWATH quantitation was attempted for all proteins in the ion library that were identified by ProteinPilot with an FDR below 1 %. The retention times of the peptides that were selected for each protein were realigned in each run according to the Internal Retention Time (iRT) peptides corresponding to the different proteins identified in each sample and eluted along the whole-time axis. The extracted ion chromatograms were then generated for each selected fragment ion; the peak areas for the peptides were obtained by summing the peak areas from the corresponding fragment ions. Protein quantization was calculated by adding the peak areas of the corresponding peptides.

The integrated peak areas (processed. mrkvw files from PeakView) were directly exported to the MarkerView software (Sciex, Redwood City, CA, USA) for relative quantitative analysis. A global normalization was carried out based on the total sum of all the peak areas extracted from all the peptides and transitions across the replicates of each sample. The average MS peak area of each protein was derived from the

replicates of the SWATH-MS of each sample followed by Student's *t*-test analysis using the MarkerView software for comparison among the samples based on the averaged area sums of all the transitions derived for each protein. The *t*-test will indicate how well each variable distinguishes the two groups, reported as a α-value. Network analysis was done with String DB 12.0 (freely available at https://string-db.org/) and SR plot software (https://www.uniprot.org/) was used for visualization. The raw data files are available in the public domain through the MassIVE repository (https://massive.ucsd.edu/ProteoSAFe/static/massive.jsp).

2.10. PET/CT acquisition and image analysis

Once the level of ocular inflammation in uveitis models and the possible existence of inflammation associated with LPS were studied, a preclinical PET/CT system (Albira PET/CT Preclinical scanner, Bruker Biospin Corp. Billerica, MA) was used to compare whole-body inflammation between both. For this purpose, a ^{18}F- FDG PET/CT study was performed in three groups of 3 rats each: FDG-C, FDG-LPSs and FDG-LPSi. Radiopharmaceutical administration was injected 24 h after uveitis induction. Animals were fasted for 12 h before the FDG PET studies.

Prior to image acquisition, glucose levels were measured before ^{18}F-FDG injection (114.67 ± 13.78 mg/dL) and then, 14.22 ± 0.37 MBq of ^{18}F-FDG was intravenously administered into the vein tail of the animals. During FDG administration and image acquisition, rats were kept anesthetized with 2.5–3 % of isoflurane/oxygen through a face mask and breathing was monitored. PET/CT static acquisitions were performed 45 min after the ^{18}F-FDG intravenous injection, consisting of 20 min PET scan followed by a 20 min CT scan. PET images were reconstructed using the Maximum Likelihood Expectation Maximization (MLEM) algorithm with 12 iterations and an image pixel size of 0.5x0.5x0.5 mm^3, including decay, scatter and random coincidences and no attenuation correction. The CT acquisition parameters were 35 kV for a tube current of 200 μA with 250 projections per bed and the reconstructed images had a pixel size of 0.5x0.5x0.5 mm^3. The Field Of View (FOV) of the PET and CT scans covered the whole body of the animals.

Image analysis was carried out using Amide's Medical Image Data Analysis Tool (Loening and Gambhir, 2003) gauging different ellipsoidal Regions Of Interest (ROIs) of 5x5x5 mm (524 mm^3) delimiting the signal area in each eye. Liver, spleen, and knee were also evaluated. The mean radiotracer concentrations derived from the different ROIs were corrected by the radioactive decay of the ^{18}F radioisotope (half-life of 110 min). The semiquantitative measurements of ^{18}F-FDG uptake were estimated using the Standardized Uptake Value (SUV) following Equation (1).

$$SUV = \frac{measured\ radioactivity\ concentration\ (Bq/mL)}{injected\ radioactivity\ (Bq)/bodyweight\ (g)} \quad (1)$$

Standardized uptake value (SUV) equation. Bq: becquerel.

2.11. Statistical analysis

Data analysis of the variables studied was carried out using GraphPad Prism 9 for macOS v.9.3.1 software (GraphPad Software, San Diego, CA, USA). Before the analysis, the normality of the distribution was checked with the Shapiro-Wilk test for each parameter studied. For IOP results, two analyses were performed: intragroup and intergroup analysis. The intragroup study was performed to observe differences within groups before and after induction or intravitreal injection. Once the assumption of normality was accepted, a parametric paired 2way ANOVA test was performed with Sidak's multiple comparisons test. Subsequently, for the intergroup analysis, a parametric nonpaired 2way ANOVA with Tukey's multiple comparisons test was applied.

For the statistical evaluation of SUV values acquired from the PET/CT scans, a one-way ANOVA with Tukey's multiple comparisons test was applied. For all cases, statistically significant differences were considered when the comparison yielded a α-value < 0.05.

3. Results

3.1. Intraocular pressure measurements (IOP)

In the intragroup comparison, the variations within the same group at the evaluated times were studied. Thus, a significant increase in intraocular pressure was observed in intravitreally LPS-induced rats (Sidak; $\alpha < 0.05$), whereas a significant decrease occurred in systemically LPS-induced rats (Sidak; $\alpha < 0.01$) (Fig. 2A). A comparison between the induced groups and the healthy control group was also performed to identify differences in IOP. A significant increase was found in postinduction measurements for the intravitreal LPS model compared to control group and between uveitis groups (Tukey, $\alpha < 0.01$). No significant differences were found between intravitreal BSS injection and the healthy control group (Tukey, α.n.s.) (Fig. 2B).

3.2. OCT image analysis

The AS-OCT enabled the anterior chamber examination, observing structural changes due to the induction of uveitis by the two routes of LPS administration, providing information on the underlying inflammation in both models. The findings observed in the images of the animals with ocular procedures were compared with images obtained from healthy control eyes (Fig. 3). Images corresponding to eyelids or skin and without a clear image of the anterior chamber were removed.

As can be seen in Fig. 3A, the anterior segment of a healthy control group (C) showed no signs of inflammation such as cellular infiltrate, fibrotic membranes or iris inflammation. The anterior chamber shows a hyporreflective images and healthy ocular structures. In the analysis of the findings of the Ci group, cellular infiltrate was found in all animals (100 %), being more prevalent in the central region. In the remaining inflammatory evaluated signs, only 10 % presented fibrotic membranes, and 20 % suffered iris inflammation in the central, middle superior and superior regions (Fig. 3B).

In the LPSs group (Fig. 3C), as a remarkable sign of inflammation, 80 % of the animals were observed to have cellular infiltrate in at least one of the five analyzed regions and 20 % suffered iris inflammation. No signs of fibrotic membranes were observed in any systemically induced animal. In the LPSi group (Fig. 3D), signs of cellular infiltrate were presented in 100 % of the animals in all regions being the central and middle superior regions the ones with the most cellular infiltrate. Fibrotic membranes and iris inflammation were found in 60 % of the animals.

After qualitative comparison of the salient signs between the Ci and LPSi groups, it was noted that the hyperreflectance of the anterior chamber of the animals in the LPSi group was higher than that observed in the Ci group, produced by the large number of cells in the anterior chamber, which in some cases agglomerated and caused cell masses. In the comparison between the signs of the LPSs model and the LPSi model, the same behavior was observed as in the previous comparison, the hyperreflectance observed in the anterior chamber of the LPSi group was still higher than that found in the LPSs group. In addition, the LPSi model produced greater inflammatory signs in the anterior chamber and to a greater degree than the LPSs model. Finally, it should be noted that the posterior segment and retina examination could not be performed due to the turbidity of the media both in the anterior chamber, as demonstrated by the AS-OCT images, and in the posterior chamber. The presence of turbidity in the ocular media prevented the proper physical functioning of the instrument and therefore it was not possible to obtain reliable and clear images of the posterior segment.

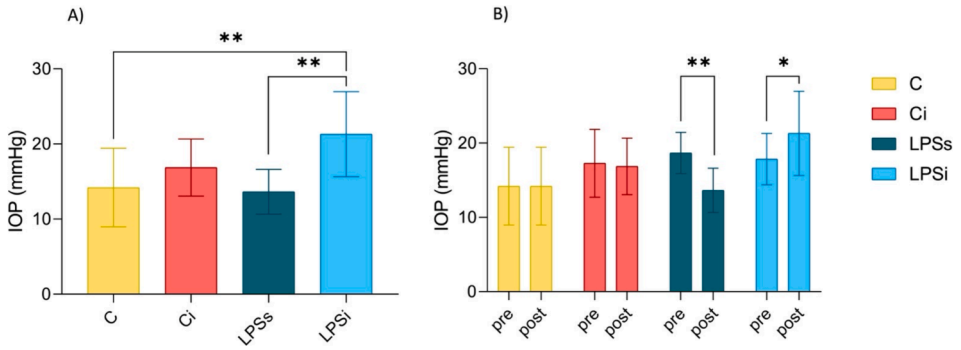

Fig. 2. Variations of intraocular pressure measured at different time-points in the different groups analyzed. A) Intragroup paired comparative analysis of intraocular pressure (Sidak's multiple comparisons test). Pre: before induction; Post: 24 h after induction. B) Intergroup unpaired comparative analysis of intraocular pressure (Tukey's multiple comparisons test); *: statistical significance $\alpha < 0.05$; **: statistical significance $\alpha < 0.01$.

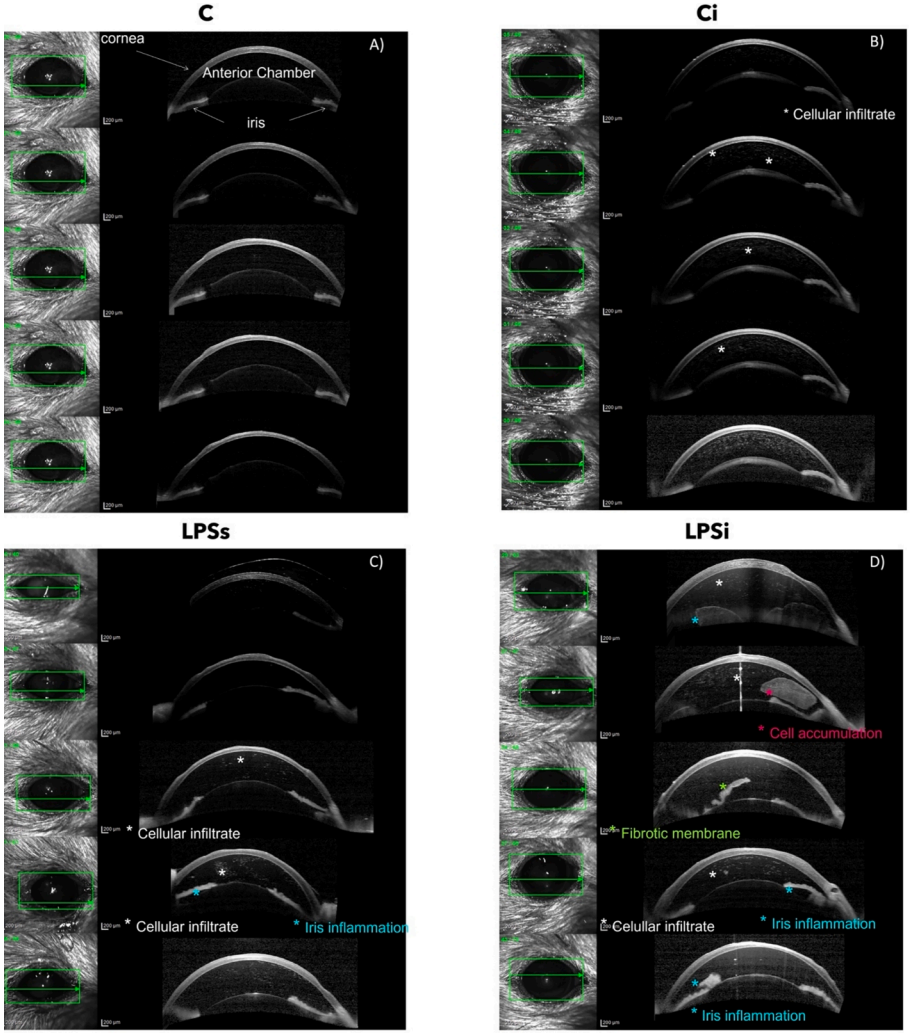

Fig. 3. *In vivo* images of the anterior chamber of the rat eye. A) Lower middle section of the anterior chamber of a healthy control rat without relevant inflammatory findings. B) Middle section of the anterior chamber of rats administered with BSS intravitreally 24 h after administration. C) Lower middle section of rats induced with systemically LPS 24 h after administration. D) Middle section of the anterior chamber of rats induced with intravitreal LPS 24 h after administration. *white: cellular infiltrate; *magenta: cell accumulation; *green: fibrotic membrane; *blue: iris inflammation.

3.3. Proteomics

A quantitative analysis of the modulated proteins was performed between the groups examined. The proteome analysis and the comparison could be found in the MassIVE repository (The comparative analysis is available in the public domain through the MassIVE repository).

A comparison was made between uveitis models (LPSi vs LPSs); healthy control group and LPSi model (C vs LPSi); healthy control group and LPSs model (C vs LPSs) and Ci group and LPSi model (Ci vs LPSi). As analysis criteria, it was studied those proteins that were statistically

significantly expressed ($\alpha < 0.05$) and with a fold change (FC) up to 2 and below 0.5.

In the LPSi vs LPSs comparison, a total of 355 proteins were quantified of which 28 have a statistically significant modulation (differentially expressed proteins: DEPs) ($\alpha < 0.05$) and the chosen ratio. Of the 28 proteins obtained, 20 of them are overexpressed at least 2-fold in the LPSi model. Fig. 4a shows a volcano plot of the modulated proteins in LPSi vs LPSs comparison. Of the 20 upregulated proteins in LPSi group, an increase was found in *S100A9* protein (FC=5.28; $\alpha < 0.05$); *Parkinson disease protein 7 homolog* (FC=4.76; $\alpha < 0.05$); *Cathepsin G* (FC=4.59; $\alpha < 0.001$); *Heat shot protein HSP 90-alpha* (FC=3.70; $\alpha < 0.05$) and *Stress-70 protein mitochondrial* (FC=2.33; $\alpha < 0.01$) among others. A network analysis of the upregulated proteins was carried out. Some of the most representative biological processes in which these proteins were involved include humoral immune response, positive regulation of defense response, response to toxic substance, inflammatory response, and response to lipids (Fig. 5).

In the analysis between the healthy control group and the LPSi model (C vs. LPSi), 29 proteins were found to be upregulated at least 2-fold in the LPSi model compared to the healthy control group (Fig. 4b). Examples of DEPs are the *Heat shock cognate 71* (FC=0.46; $\alpha < 0.01$), *Stress 70 protein* (FC=0.43; $\alpha < 0.05$), *Gamma crystallin N* (FC=0.39; $\alpha < 0.05$), *gamma crystallin S* (FC=0.32; $\alpha < 0.05$), *Gamma crystallin B* (FC=0.24; $\alpha < 0.05$), *Gamma crystallin C* (FC=0.16; $\alpha < 0.05$), *protein S100-A8* (FC=0.31; $\alpha < 0.01$), *Ig gamma-2B chain* (FC=0.28; $\alpha < 0.05$), *Cathepsin G* (FC=0.16; $\alpha < 0.001$), *serine protease inhibition* (FC=0.13; $\alpha < 0.01$), *serotransferrin* (FC=0.11; $\alpha < 0.05$), *protein S100-A9* (FC=0.09; $\alpha < 0.05$), *complement C3* (FC=0.09; $\alpha < 0.01$), among others. As revealed by network analysis different biological processes were found significantly altered such as neutrophil aggregation, very-low-density lipoprotein particle remodeling, regulation of Cdc42 protein signal transduction, high-density lipoprotein particle remodeling, acute inflammatory response, humoral immune response, response to wounding, wound healing, regulation of inflammatory response, inflammatory response, innate immune response and regulation of immune response, among others (Fig. 6). When comparing the Ci model and LPSi (Ci vs LPSi) 24 DEPs were found. Overlapping DEPs were detected after crossing the C vs LPSi and Ci vs LPSi results. The upregulated LPSi proteins present in both comparisons were *Cathepsin G* (FC=0.25; $\alpha < 0.001$), *Protein S100-A8* (FC=0.24; $\alpha < 0.001$), *Serine protease inhibitor A3N* (FC=0.26; $\alpha < 0.001$) and *Complement C3* (FC=0.21; $\alpha < 0.05$).

When comparing the healthy control group versus LPSs group (C vs. LPSs) only 8 proteins were significantly upregulated and within the ratio chosen in the LPSs group (Fig. 4c). *Complement C3* (FC=0.28; $\alpha < 0.001$) and *serine protease inhibitor* (FC=0.25; $\alpha < 0.001$) were found among the upregulated proteins.

3.4. PET/CT studies

The mean uptake of ^{18}F-FDG of each selected organ was analyzed individually and a multiple comparative analysis was performed between the results obtained in healthy control rats and those injected with LPS systemically and intravitreally. The eyes uptake of ^{18}F-FDG PET/CT images in the differents groups are shown in Fig. 7. The red ellipses in the image represent the ROIs of the eyes. In this first qualitative evaluation, a greater uptake of ^{18}F-FDG is clearly seen in the brain of the FDG-LPSi group compared to the other two groups, although the uptake of the FDG-LPSs group is greater than the FDG-C group. Furthermore, in the FDG-LPSs group, greater bone and joint uptake was observed.

As shown in Fig. 8, a significant difference between the healthy control rats and the induced uveitis models for the ocular region analysis was observed. Both uveitis models gave significantly higher SUV values than control rats (Tukey, $\alpha < 0.0001$). In the comparison between LPSi and LPSs induced rats, the uptake of ^{18}F-FDG in the LPSi group is significantly higher than in the LPSs group (Tukey, $\alpha < 0.05$).

Systemic uptake of ^{18}F-FDG was evaluated in different regions. As can be seen in Fig. 8, there was notable uptake in the liver, spleen, and knee. In the comparative analysis between healthy control group and the induced groups, a significantly higher SUV was found in the liver of the induced models compared to the healthy control rat (Tukey, $\alpha_{intravitreal} < 0.001$; $\alpha_{systemic} < 0.0001$). Significant differences in uptake were also found between the intravitreal and systemic induced model in spleen, with SUV being higher in the systemic model (Tukey, $\alpha < 0.0001$).

The knee was another region where increased uptake was observed. In this area, induced uveitis rats gave significantly higher SUV values than healthy control rats. Again, there were significant differences between systemic and intravitreal-induced animals, with the systemic group giving significantly higher SUV values than the intravitreal group (Tukey, $\alpha < 0.001$). As can be seen in Fig. 7, the ^{18}F-FDG uptake in the brain is higher in the uveitis model groups, and among them, the FDG-LPSi group is the one with the highest uptake.

4. Discussion

In this study, two models of uveitis were analyzed and characterized with novel and noninvasive imaging techniques. Moreover, a proteomic study was performed to correlate imaging findings with the presence of certain inflammation-modulating proteins. Uveitis model induction was performed through the administration of an endotoxin by two different routes (Zhang et al., 2022). First, a systemic route is considered as it is the one that has traditionally been used to induce uveitis models. This involves a rapid and short course of anterior uveitis (Bansal et al., 2015) due to the privileged and unique immune system of the eyeball (Egwuagu et al., 2021; Mölzer et al., 2021). When LPS is administered systemically, the lipopolysaccharide breaks the blood barriers and

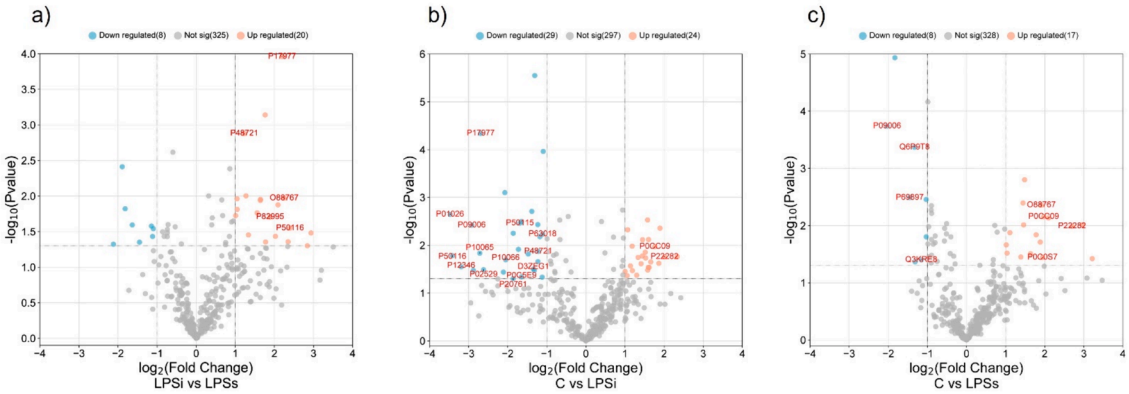

Fig. 4. Volcano plot of the modulated proteins in the differents comparisons. a) LPSi vs LPSs; b) C vs LPSi and c) C vs LPSs.

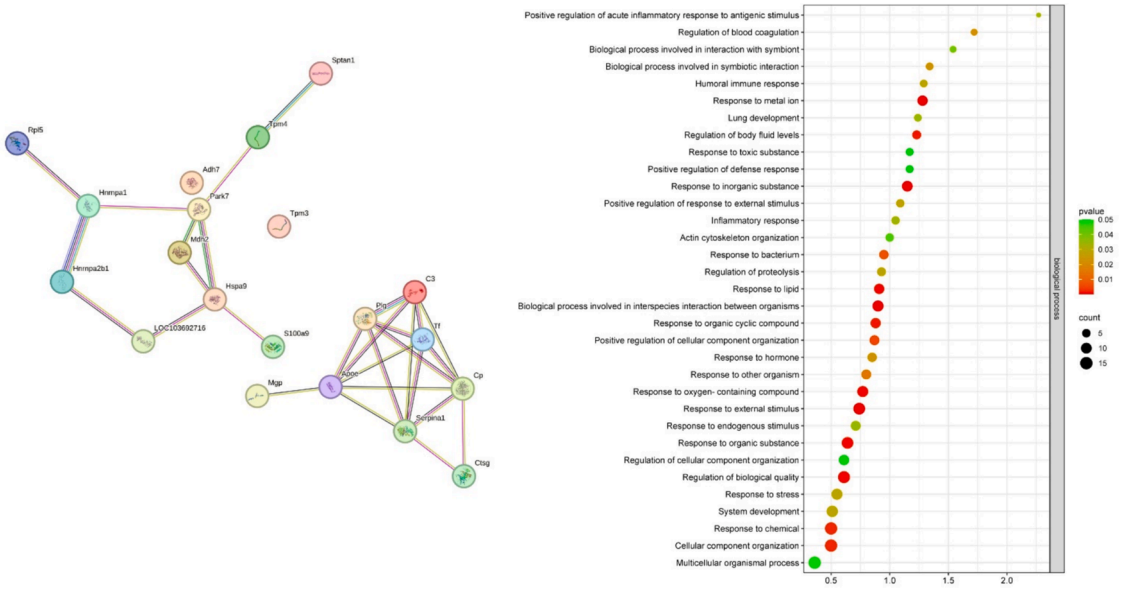

Fig. 5. Network and gene ontology analysis of the comparison LPSi vs LPSs.

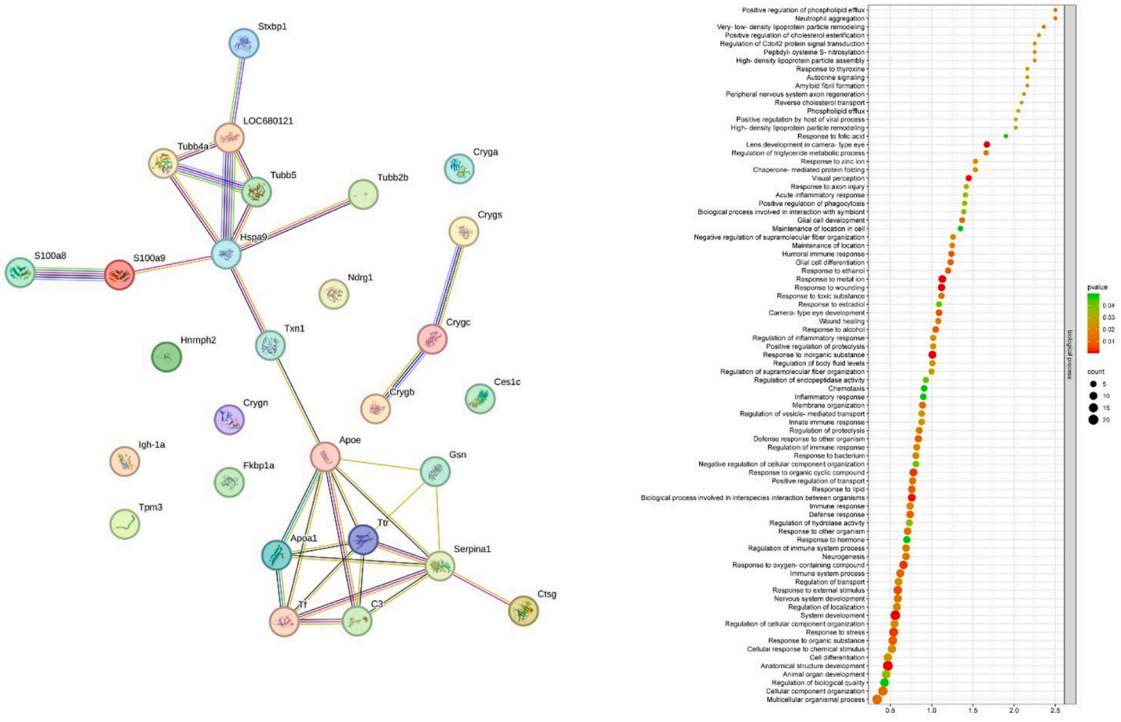

Fig. 6. Network and gene ontology analysis of the comparison C vs LPSi.

triggers the activation of the immune system. At that time, immune cells initiate migration to the anterior segment of the eye and other structures (Egwuagu et al., 2021). This phenomenon allows systemic administration of LPS to be used to evaluate ocular and other inflammatory processes such as neuroinflammation (Di Paolo et al., 2023; Md Pisar et al., 2023) or gastrointestinal dysmotility sepsis (Castro et al., 2023), etc.) despite its handling and reproducibility (Garg et al., 2021). Nevertheless, systemic administration of LPS can induce systemic inflammatory mechanisms that would mask or hinder ocular evaluation (Arıkan et al., 2023; Gupta et al., 2008). Due to this, more and more studies are choosing intravitreal administration over systemic administration (Garg et al., 2021; Rosenbaum et al., 2011). Although these models do not provoke all the ocular signs of clinical uveitis (Chu et al., 2016), it seems that the induced inflammation should be only local and therefore more appropriate for a uveitis model. This is the reason because intravitreal administration is considered as preferred induction model to study acute anterior uveitis and it might be the most appropriate model to evaluate the efficacy of ocular drugs, since it presents increased levels of proinflammatory cytokines in ocular fluids (Herbort et al., 1989). Despite the intense work in generating optimal models of uveitis, there has been little progress in the development of noninvasive biomarkers. Today, there is a growing interest in less invasive techniques for the evaluation and characterization of uveitis, mainly due to the need for improved *in vivo* characterization of the current models and ultimately for a better

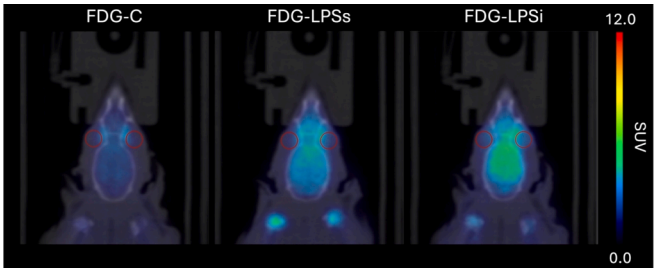

Fig. 7. Coronal fused PET/CT images of rats head for the three groups scanned. The color scale represented the uptake of ^{18}F-FDG from lower (blue) to higher (red) intensity.

understanding of the uveitis behavior. In addition, more ethical alternatives are required in preclinical research, due to the increasingly stringent limitations on the use of animals for experimentation. The imaging studies implemented in this work have a direct impact on the implications of the 3Rs, since the number of animals is exponentially reduced by not having to sacrifice each animal to measure the studied parameters. Regarding to this, present study provides a full characterization of uveitis models induced by systemic and intravitreal administration of LPS using *in vivo* imaging biomarkers based on OCT and PET/CT studies. Furthermore, imaging findings were correlated with an extensive proteomic study, which allowed the previous molecular characterization of the models in terms of inflammation-modulating proteins.

High IOP increases the likelihood of axonal damage and, consequently, glaucoma. Over the years, the need to study IOP in patients with uveitis has been increasing due to its association (Friedman et al., 2013; Herbert et al., 2004; Kothari et al., 2015). In this work, when studying IOP variations, it is observed that intravitreal injection of LPS causes a significant increase that is not observed in the systemic model. This finding could be due to the immediate increase due to the injection itself observed in different studies (Grzybowski et al., 2018; Lemos et al., 2015). Consequently, the IOP increase of the intravitreal-induced model could be caused by the combined influence between the severe ocular inflammatory process and the effect of the intravitreal injection itself. Del Sole *et al.* reported in a study of intravitreal injection uveitis in cats, an increase in IOP after injection of sterile saline (Sole et al., 2008). In this regard, the differences found between Sole *et al.* study and ours may be due to possible differences in the immune response between cats and rats. Our hypothesis is that the inflammation caused by LPS injection causes a continued change in IOP, since no differences were found between BSS injection and control animals either. Regarding AS-OCT studies, the use of this imaging technique provided noninvasive information on morphological slices of the animal's anterior chamber. This allowed us to detect clinical signs of cellular infiltrate, fibrotic membrane and iris inflammation in both intravitreal and systemic LPS-induced animals, results that correspond with those found in other preclinical studies of the disease (Chen et al., 2013; Choi et al., 2015; Downie et al., 2014; Gutowski et al., 2017). Fundus images and retinal OCT images could not be obtained due to underlying inflammation and turbidity in the posterior chamber, especially in those induced intravitreally. This event was also observed in other studies confirming the presence of ocular media opacity (Chen and Caspi, 2019). Moreover, it was observed that intravitreal injection of BSS produced clear signs of intraocular inflammation. These findings are consistent with previous clinical reports of possible subclinical inflammation in the anterior chamber after the injection (Sole et al., 2008). Finally, it has been confirmed that intravitreal administration of LPS effectively activates the cellular inflammatory response, leading to increased production and release of proinflammatory cells, as described by Gupta *et al.* (Gupta et al., 2008).

Our study describes the proteomic profile obtained in the different models. It was demonstrated the presence of histones, crystalline proteins and S100A9 in the uveitis models, with higher expression when LPS is administered intravitreally. In addition, it has been proved that the presence of S100A8, a protein that has been described as specific in several animal models of uveitis, and proinflammatory proteins such as Cathepsin G, Serine protease inhibitor A3N and Complement C3 proteins in the eye are related to the presence of LPS. Among the proinflammatory proteins established in the uveitis models, the Parkinson's disease protein 7 homologue was more upregulated in the intravitreal model, although it was found in both EIU models. This protein has a protective function against oxidative stress and mediator of inflammation by TLR4 receptor (Lippai et al., 2021). These results are in agreement with previous results in the proteome characterization of animal models, where the presence of beta-B2-crystallin (Rao et al., 2008), αA-Crystallin (Wang et al., 2015), S100A8 and S100A9 protein (Pepple et al., 2015) were also determined. There are also studies in aqueous humor demonstrating increased levels of calprotectin and apolipoprotein E in inflammation models, as well as beta-B2-crystallin (Zhang et al., 2022). Zhang *et al.* identified histones such as H1, H2A and H2B at the disease peak. They concluded that the presence of histones in the animals retina could lead to a protective effect against LPS (Zhang et al., 2022).

After establishing the proteomic characterization of the models confirming the association between LPS administration and ocular inflammation, ^{18}F-FDG PET/CT study was subsequently conducted. To our knowledge, this is the first study using PET/CT to characterize the inflammation of EIU models both in the eye and whole-body organism. PET/CT results are in accordance with those obtained in AS-OCT and proteomic studies. The uveitis model induced through intravitreal injection generates a greater ocular inflammation compared to the systematically induced model. According to the results, the analysis performed in the liver, spleen and knee shows that ^{18}F-FDG uptake is higher when LPS is administered systemically, confirming a greater

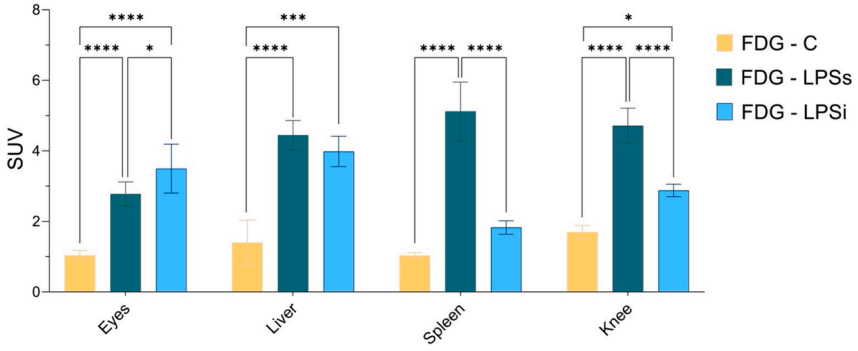

Fig. 8. SUV values and standard deviation of the evaluated organs in the different performed models and their comparison between groups. *: $\alpha < 0.05$; ***: $\alpha < 0.001$ and ****: $\alpha < 0.0001$.

affectation of these organs. In conclusion, the inflammation caused in the systemic model is more generalized than that obtained after local administration of LPS. This imaging technique was also used by Fujii *et al.* (Fujii et al., 2018) for evaluating response of ocular adnexal lymphoma to treatment and by Bazewicz *et al.* (Bazewicz et al., 2023) in the work-up of children with uveitis. Rodents, unlike humans, have a gland in the head, called Harderian gland, which uptakes a large amount of ^{18}F-FDG. This structure is located very close to the eye of the rats, so special care must be taken to ensure that the uptake data from the eye is independent of, and not affected by, the uptake of the gland. For this reason, when performing the image analysis and placing the ocular ROIs it was verified that the eye data were not influenced by the spillover uptake of the Harderian gland. The retina has been described as a window to the brain because the axons that compose the optic nerve are directly connected to the brain. This makes the optic nerve a transport pathway to the cerebrospinal fluid (Wang et al., 2020). When LPS is administered, blood-ocular barriers are breached and the inflammatory cascade is activated leading to cytokine proliferation and activation of microglia (Kokona et al., 2018; Lai et al., 2022). These events may explain the increased ^{18}F-FDG uptake in the brain of animals administered LPS intravitreally.

Among the limitations of our study is the subjective evaluation of OCT images. There are studies that propose objective assessment algorithms for anterior chamber evaluation (Xu et al., 2017). In clinical practice, one of the signs that is checked is possible corneal edema. In our case, it could not be evaluated because the Spectralis OCT software available to us does not present an automatic segmentation of the cornea. Due to the manual measurement of corneal edema, its possible error in measurement accuracy and the fact that corneal thickness is the least reliable sign of inflammation, it was decided not to perform it. Another limitation for IOP and OCT is the duration of anesthesia. Studies have shown that prolonged anesthesia can cause opacities and ocular dryness (Bell et al., 2019). Despite the instillation of artificial tears, changes in imaging phase are observed, probably due to anesthesia. Although the performed studies demonstrate the usefulness of OCT to observe changes in animal model inflammation and correlation between the tested assays, it would be interesting to objectify the OCT results with histological studies.

The results of each study in this work are consistent with each other. The high presence of proteins belonging to the cells that play a key role in the inflammatory process obtained in the proteomic study corresponds with the results obtained in the OCT and PET/CT images, where an increase in cellular infiltration and iris inflammation, and a higher uptake of ^{18}F-FDG caused by inflammation, respectively, can be seen. Taking into account that the degree of inflammation from highest to lowest of the studied groups is LPSi, LPSs and healthy, it is possible to correlate the level of expression of the proteins obtained by proteomics with the appearance of signs through OCT and the level of ^{18}F-FDG uptake in the PET/CT study.

5. Conclusions

Our study has provided noninvasive imaging of two animal models of uveitis, establishing Spectralis AS-OCT is a useful and noninvasive tool for anterior ocular segment assessment in experimental models. In turn, PET/CT studies with ^{18}F-FDG may be of potential interest as a noninvasive biomarker in ocular diseases. The differences between the uveitis models induced by intravitreal and systemic administration of LPS have been characterized, confirming that the intravitreal model generates more inflammation in the anterior chamber in all the performed studies, whereas the systemic model could better reproduce the conditions of a generalized inflammation affecting other parts of the organism. These results would provide useful information for application in future specific inflammatory diseases and pharmacological studies.

CRediT authorship contribution statement

Andrea Cuartero-Martínez: Data curation, Formal analysis, Investigation, Methodology, Validation, Visualization, Writing – original draft, Writing – review & editing. **Xurxo García-Otero:** Conceptualization, Data curation, Formal analysis, Investigation, Methodology, Validation, Visualization, Writing – original draft, Writing – review & editing. **Jessica Codesido:** Data curation, Formal analysis, Investigation, Methodology, Writing – review & editing. **Noemí Gómez-Lado:** Methodology, Writing – review & editing. **Jesús Mateos:** Methodology, Supervision, Writing – review & editing. **Susana B. Bravo:** Data curation, Formal analysis, Methodology. **Carmen Antía Rodríguez-Fernández:** Methodology, Validation, Writing – review & editing. **Miguel González-Barcia:** Conceptualization, Resources, Validation, Writing – review & editing. **Pablo Aguiar:** Funding acquisition, Methodology, Resources, Supervision, Validation, Visualization, Writing – review & editing. **Marcos Ortega-Hortas:** Conceptualization, Funding acquisition, Project administration, Resources, Supervision, Visualization, Writing – review & editing. **Francisco J. Otero-Espinar:** Conceptualization, Formal analysis, Funding acquisition, Project administration, Resources, Supervision, Visualization, Writing – review & editing. **Anxo Fernández-Ferreiro:** Conceptualization, Funding acquisition, Project administration, Resources, Supervision, Visualization, Writing – review & editing.

Declaration of competing interest

The authors declare that they have no known competing financial interests or personal relationships that could have appeared to influence the work reported in this paper.

Data availability

Data will be made available on request.

Acknowledgement

This work was partially supported by Instituto de Salud Carlos III (ISCIII, Spain) through PI20/00719 project, Axencia Galega de Innovación (Grupos de Potencial Crecimiento IN607B2020/11, Spain), Ministry of Science and Innovation of Spain (MICINN, Spain) through PID2022-142350OB-C21 project and Xunta de Galicia (Grupo de Referencia Competitiva, ED431C 2021/26, Spain). X. García-Otero and J. Mateos acknowledges the support of Xunta de Galicia (Spain) through the postdoctoral fellowship [ED481B-2023-063] and Senior Talent Research grant [11-IN858A_2021_1141142]. J. Codesido is grateful to the Health Research Institute of Santiago de Compostela (IDIS, Spain) for financing his predoctoral research fellowship.

References

Agarwal, A., Invernizzi, A., 2022. The role of optical coherence tomography and optical coherence tomography angiography in the differential diagnosis of posterior uveitis. Ocul Immunol Inflamm 30, 682–689. https://doi.org/10.1080/09273948.2022.2071743.

Arıkan, S., Guven, S., Sehitoglu, M.H., Elmas, S., 2023. The possible effect of topically applied azithromycin and moxifloxacin on the alleviation of uveitis. Int Ophthalmol 43, 4451–4460. https://doi.org/10.1007/s10792-023-02845-5.

Arras, M., Autenried, P., Rettich, A., Spaeni, D., Rülicke, T., 2001. Optimization of intraperitoneal injection anesthesia in mice: drugs, dosages, adverse effects, and anesthesia depth. Comp Med 51, 443–456.

ARVO, 2021. The Association for Research in Vision and Ophthalmology- Statement for the Use of Animals in Ophthalmic and Vision Research [WWW Document]. URL https://www.arvo.org/About/policies/statement-for-the-use-of-animals-in-ophthalmic-and-vision-research/ (accessed 5.22.23).

Aumann, S., Donner, S., Fischer, J., Müller, F., 2019. Optical coherence tomography (OCT): Principle and technical realization. In: Bille, J.F. (Ed.), High Resolution Imaging in Microscopy and Ophthalmology. Springer International Publishing, Cham, pp. 59–85. https://doi.org/10.1007/978-3-030-16638-0_3.

Bansal, S., Barathi, V.A., Iwata, D., Agrawal, R., 2015. Experimental autoimmune uveitis and other animal models of uveitis: An update. Indian J Ophthalmol 63, 211–218. https://doi.org/10.4103/0301-4738.156914.
Bansal, R., Gupta, A., 2020. Protein biomarkers in uveitis. Front Immunol 11, 610428. https://doi.org/10.3389/fimmu.2020.610428.
Bazewicz, M., Makhoul, D., Goffin, L., El Mouden, J., Judice M Relvas, L., Caspers, L., Draganova, D., Postelmans, L., Garcia, C., Willermain, F., 2023. Clinical utility of 18F-FDG PET/CT in the work-up of children with uveitis. Ocul Immunol Inflamm 31, 77–86. https://doi.org/10.1080/09273948.2021.1985522.
Bell, B.A., Bonilha, V.L., Hagstrom, S.A., Anand-Apte, B., Hollyfield, J.G., Samuels, I.S., 2019. Prolonged ocular exposure leads to retinal lesions in mice. Exp Eye Res 185, 107672. https://doi.org/10.1016/j.exer.2019.05.012.
Bermudez, M.A., Sendon-Lago, J., Seoane, S., Eiro, N., Gonzalez, F., Saa, J., Vizoso, F., Perez-Fernandez, R., 2016. Anti-inflammatory effect of conditioned medium from human uterine cervical stem cells in uveitis. Exp Eye Res 149, 84–92. https://doi.org/10.1016/j.exer.2016.06.022.
Castro, M., Valero, M.S., López-Tofiño, Y., López-Gómez, L., Girón, R., Martín-Fontelles, M.I., Uranga, J.A., Abalo, R., 2023. Radiographic and histopathological study of gastrointestinal dysmotility in lipopolysaccharide-induced sepsis in the rat. Neurogastroenterol. Motil. 35, e14639. https://doi.org/10.1111/nmo.14639.
Chang, M.H., Shantha, J.G., Fondriest, J.J., Lo, M.S., Angeles-Han, S.T., 2021. Uveitis in children and adolescents. Rheum Dis Clin North Am 47, 619–641. https://doi.org/10.1016/j.rdc.2021.07.005.
Chen, J., Caspi, R.R., 2019. Clinical and Functional Evaluation of Ocular Inflammatory Disease Using the Model of Experimental Autoimmune Uveitis. Methods Mol Biol 1899, 211–227. https://doi.org/10.1007/978-1-4939-8938-6_15.
Chen, J., Qian, H., Horai, R., Chan, C.-C., Caspi, R.R., 2013. Use of optical coherence tomography and electroretinography to evaluate retinal pathology in a mouse model of autoimmune uveitis. PLoS One 8, e63904. https://doi.org/10.1371/journal.pone.0063904.
Choi, W.J., Pepple, K.L., Zhi, Z., Wang, R.K., 2015. Optical coherence tomography based microangiography for quantitative monitoring of structural and vascular changes in a rat model of acute uveitis in vivo: a preliminary study. J Biomed Opt 20, 016015. https://doi.org/10.1117/1.JBO.20.1.016015.
Choi, W.J., Pepple, K.L., Wang, R.K., 2018. Automated 3-D cell counting method for grading uveitis of rodent eye in vivo with optical coherence tomography. J Biophotonics 11, e201800140. https://doi.org/10.1002/jbio.201800140.
Chu, C.J., Gardner, P.J., Copland, D.A., Liyanage, S.E., Gonzalez-Cordero, A., Kleine Holthaus, S.-M., Luhmann, U.F.O., Smith, A.J., Ali, R.R., Dick, A.D., 2016. Multimodal analysis of ocular inflammation using the endotoxin-induced uveitis mouse model. Dis Model Mech 9, 473–481. https://doi.org/10.1242/dmm.022475.
Crișan, G., Moldovean-Cioroianu, N.S., Timaru, D.-G., Andrieș, G., Căinap, C., Chiș, V., 2022. Radiopharmaceuticals for PET and SPECT Imaging: A literature review over the last decade. Int J Mol Sci 23, 5023. https://doi.org/10.3390/ijms23095023.
da Silva, P.S., Girol, A.P., Oliani, S.M., 2011. Mast cells modulate the inflammatory process in endotoxin-induced uveitis. Mol vis 17, 1310–1319.
Di Paolo, M., Corsi, F., Cerri, C., Bisti, S., Piano, I., Gargini, C., 2023. A Window to the brain: The retina to monitor the progression and efficacy of saffron repron® pre-treatment in an LPS model of neuroinflammation and memory impairment. Pharmaceuticals (Basel) 16, 1307. https://doi.org/10.3390/ph16091307.
Downie, L.E., Stainer, M.J., Chinnery, H.R., 2014. Monitoring of strain-dependent responsiveness to TLR activation in the mouse anterior segment using SD-OCT. Invest Ophthalmol vis Sci 55, 8189–8199. https://doi.org/10.1167/iovs.14-15595.
Egwuagu, C.E., Alhakeem, S.A., Mbanefo, E.C., 2021. Uveitis: Molecular pathogenesis and emerging therapies. Front Immunol 12, 623725. https://doi.org/10.3389/fimmu.2021.623725.
Fan, N.-W., Li, J., Mittal, S.K., Foulsham, W., Elbasiony, E., Huckfeldt, R.M., Chauhan, S. K., Chen, Y., 2021. Characterization of clinical and immune responses in an experimental chronic autoimmune uveitis model. Am J Pathol 191, 425–437. https://doi.org/10.1016/j.ajpath.2020.09.004.
Fernández-Ferreiro, A., Luaces-Rodríguez, A., Aguiar, P., Pardo-Montero, J., González-Barcia, M., García-Varela, L., Herranz, M., Silva-Rodríguez, J., Gil-Martínez, M., Bermúdez, M.A., Vieites-Prado, A., Blanco-Méndez, J., Lamas, M.J., Gómez-Ulla, F., Ruibal, Á., Otero-Espinar, F.J., González, F., 2017. Preclinical PET study of intravitreal injections. Invest Ophthalmol vis Sci 58, 2843–2851. https://doi.org/10.1167/iovs.17-21812.
Friedman, D.S., Holbrook, J.T., Ansari, H., Alexander, J., Burke, A., Reed, S.B., Katz, J., Thorne, J.E., Lightman, S.L., Kempen, J.H., 2013. Risk of elevated intraocular pressure and glaucoma in patients with uveitis; results of the multicenter uveitis steroid treatment trial. Ophthalmology 120, 1571–1579. https://doi.org/10.1016/j.ophtha.2013.01.025.
Fujii, H., Tanaka, H., Nomoto, Y., Harata, N., Oota, S., Isogai, J., Yoshida, K., 2018. Usefulness of 18F-FDG PET/CT for evaluating response of ocular adnexal lymphoma to treatment. Medicine (Baltimore) 97, e0543. https://doi.org/10.1097/MD.0000000000010543.
Gadjanski, I., Williams, S.K., Hein, K., Sättler, M.B., Bähr, M., Diem, R., 2011. Correlation of optical coherence tomography with clinical and histopathological findings in experimental autoimmune uveoretinitis. Exp Eye Res 93, 82–90. https://doi.org/10.1016/j.exer.2011.04.012.
García-Otero, X., Mondelo-García, C., González, F., Perez-Fernandez, R., Avila, L., Antúnez-López, J.R., González-Barcia, M., Adan, A., Aguiar, P., Otero-Espinar, F.J., Bermúdez, M.A., Fernández-Ferreiro, A., 2021. Anti-inflammatory effect of tacrolimus/hydroxypropyl-β-cyclodextrin eye drops in an endotoxin-induced uveitis model. Pharmaceutics 13, 1737. https://doi.org/10.3390/pharmaceutics13101737.
García-Otero, X., Mondelo-García, C., Bandín-Vilar, E., Gómez-Lado, N., Silva-Rodríguez, J., Rey-Bretal, D., Victoria Otero-Espinar, M., Adan, A., González-Barcia, M., Aguiar, P., Otero-Espinar, F.J., Fernández-Ferreiro, A., 2022. PET study of intravitreal adalimumab pharmacokinetics in a uveitis rat model. Int. J. Pharm. 627, 122261 https://doi.org/10.1016/j.ijpharm.2022.122261.
Garg, V., Nirmal, J., Riadi, Y., Kesharwani, P., Kohli, K., Jain, G.K., 2021. Amelioration of endotoxin-induced uveitis in rabbit by topical administration of tacrolimus proglycosome nano-vesicles. J Pharm Sci 110, 871–875. https://doi.org/10.1016/j.xphs.2020.10.060.
Girol, A.P., Mimura, K.K.O., Drewes, C.C., Bolonheis, S.M., Solito, E., Farsky, S.H.P., Gil, C.D., Oliani, S.M., 2013. Anti-inflammatory mechanisms of the annexin A1 protein and its mimetic peptide Ac2-26 in models of ocular inflammation in vivo and in vitro. J Immunol 190, 5689–5701. https://doi.org/10.4049/jimmunol.1202030.
Glaudemans, A.W.J.M., de Vries, E.F.J., Galli, F., Dierckx, R.A.J.O., Slart, R.H.J.A., Signore, A., 2013. The use of (18)F-FDG-PET/CT for diagnosis and treatment monitoring of inflammatory and infectious diseases. Clin Dev Immunol 2013, 623036. https://doi.org/10.1155/2013/623036.
Grzybowski, A., Told, R., Sacu, S., Bandello, F., Moisseiev, E., Loewenstein, A., Schmidt-Erfurth, U., Board, E., 2018. 2018 Update on intravitreal injections: Euretina expert consensus recommendations. Ophthalmologica 239, 181–193. https://doi.org/10.1159/000486145.
Gupta, S.K., Agarwal, R., Srivastava, S., Agarwal, P., Agrawal, S.S., Saxena, R., Galpalli, N., 2008. The anti-inflammatory effects of curcuma longa and berberis aristata in endotoxin-induced uveitis in rabbits. Invest. Ophthalmol. Vis. Sci. 49, 4036–4040. https://doi.org/10.1167/iovs.07-1186.
Gutowski, M.B., Wilson, L., Van Gelder, R.N., Pepple, K.L., 2017. In vivo bioluminescence imaging for longitudinal monitoring of inflammation in animal models of uveitis. Invest Ophthalmol vis Sci 58, 1521–1528. https://doi.org/10.1167/iovs.16-20824.
Herbert, H.M., Viswanathan, A., Jackson, H., Lightman, S.L., 2004. Risk factors for elevated intraocular pressure in uveitis. J Glaucoma 13, 96–99. https://doi.org/10.1097/00061198-200404000-00003.
Herbort, C.P., Okumura, A., Mochizuki, M., 1989. Immunopharmacological analysis of endotoxin-induced uveitis in the rat. Exp. Eye Res. 48, 693–705. https://doi.org/10.1016/0014-4835(89)90010-9.
Imai, H., Ohta, K., Yoshida, A., Suzuki, S., Hashizume, K., Usami, S., Kikuchi, T., 2010. {mu}-Crystallin, new candidate protein in endotoxin-induced uveitis. Invest Ophthalmol vis Sci 51, 3554–3559. https://doi.org/10.1167/iovs.09-3728.
Invernizzi, A., Cozzi, M., Staurenghi, G., 2019. Optical coherence tomography and optical coherence tomography angiography in uveitis: A review. Clin. Experiment. Ophthalmol. 47, 357–371. https://doi.org/10.1111/ceo.13470.
Jabs, D.A., Nussenblatt, R.B., Rosenbaum, J.T., 2005. Standardization of uveitis nomenclature for reporting clinical data. Results of the First International Workshop. Am J Ophthalmol 140, 509–516. https://doi.org/10.1016/j.ajo.2005.03.057.
Kokona, D., Ebneter, A., Escher, P., Zinkernagel, M.S., 2018. Colony-stimulating factor 1 receptor inhibition prevents disruption of the blood-retina barrier during chronic inflammation. J Neuroinflammation 15, 340. https://doi.org/10.1186/s12974-018-1373-4.
Kothari, S., Foster, C.S., Pistilli, M., Liesegang, T.L., Daniel, E., Sen, H.N., Suhler, E.B., Thorne, J.E., Jabs, D.A., Levy-Clarke, G.A., Nussenblatt, R.B., Rosenbaum, J.T., Lawrence, S.D., Kempen, J.H., 2015. The risk of intraocular pressure elevation in pediatric non-infectious uveitis. Ophthalmology 122, 1987–2001. https://doi.org/10.1016/j.ophtha.2015.06.041.
Lai, W., Huang, J., Fang, W., Deng, S., Xie, Y., Wang, W., Qiao, T., Xu, G., Wang, X., Ding, F., 2022. Optic nerve head: A gatekeeper for vitreous infectious insults? Front Immunol 13, 987771. https://doi.org/10.3389/fimmu.2022.987771.
Lemos, V., Cabugueira, A., Noronha, M., Abegão Pinto, L., Reina, M., Branco, J., Gomes, T., 2015. Intraocular pressure in eyes receiving intravitreal antivascular endothelial growth factor injections. Ophthalmologica 233, 162–168. https://doi.org/10.1159/000369478.
Lippai, R., Veres-Székely, A., Sziksz, E., Iwakura, Y., Pap, D., Rokonay, R., Szebeni, B., Lotz, G., Béres, N.J., Cseh, Á., Szabó, A.J., Vannay, Á., 2021. Immunomodulatory role of parkinson's disease 7 in inflammatory bowel disease. Sci Rep 11, 14582. https://doi.org/10.1038/s41598-021-93671-1.
Loening, A.M., Gambhir, S.S., 2003. AMIDE: a free software tool for multimodality medical image analysis. Mol Imaging 2, 131–137. https://doi.org/10.1162/153535002003033.
López-López, M., Regueiro, U., Bravo, S.B., Chantada-Vázquez, M.del.P., Varela-Fernández, R., Ávila-Gómez, P., Hervella, P., Lema, I., 2021. Tear proteomics in keratoconus: A quantitative SWATH-MS analysis. Invest Ophthalmol vis Sci 62, 30. https://doi.org/10.1167/iovs.62.10.30.
Luaces-Rodríguez, A., del Amo, E.M., Mondelo-García, C., Gómez-Lado, N., Gonzalez, F., Ruibal, Á., González-Barcia, M., Zarra-Ferro, I., Otero-Espinar, F.J., Fernández-Ferreiro, A., Aguiar, P., 2020. PET study of ocular and blood pharmacokinetics of intravitreal bevacizumab and aflibercept in rats. Eur. J. Pharm. Biopharm. 154, 330–337. https://doi.org/10.1016/j.ejpb.2020.06.024.
Mateos, J., Fernández Pernas, P., Fafián Labora, J., Blanco, F., Arufe, M.del.C., 2014. Proteomic applications in the study of human mesenchymal stem cells. Proteomes 2, 53–71. https://doi.org/10.3390/proteomes2010053.
Md Pisar, M., Chee, B.J., Long, I., Osman, A., 2023. Protective effects of Centella asiatica extract on spatial memory and learning deficits in animal model of systemic inflammation induced by lipopolysaccharide. Annals of Medicine 55 (1), 2224970. https://doi.org/10.1080/07853890.2023.2224970.
Mérida, S., Palacios, E., Navea, A., Bosch-Morell, F., 2015. Macrophages and uveitis in experimental animal models. Mediators Inflamm 2015, 671417. https://doi.org/10.1155/2015/671417.

Mölzer, C., Heissigerova, J., Wilson, H.M., Kuffova, L., Forrester, J.V., 2021. Immune privilege: The microbiome and uveitis. Front Immunol 11, 608377. https://doi.org/10.3389/fimmu.2020.608377.

National Research Council (US), 2011. Guide for the Care and Use of Laboratory Animals, 8th ed, The National Academies Collection: Reports funded by National Institutes of Health. National Academies Press (US), Washington (DC).

Pepple, K.L., Rotkis, L., Wilson, L., Sandt, A., Van Gelder, R.N., 2015. Comparative proteomic analysis of two uveitis models in lewis rats. Invest Ophthalmol vis Sci 56, 8449–8456. https://doi.org/10.1167/iovs.15-17524.

Pepple, K.L., Choi, W.J., Wilson, L., Van Gelder, R.N., Wang, R.K., 2016. Quantitative assessment of anterior segment inflammation in a rat model of uveitis using spectral-domain optical coherence tomography. Invest Ophthalmol vis Sci 57, 3567–3575. https://doi.org/10.1167/iovs.16-19276.

Pichi, F., Curi, A.L.L., Vasconcelos-Santos, D.V., Marchese, A., Cicinelli, M.V., Miserocchi, E., Schlaen, A., 2022. Optical coherence tomography findings in infectious posterior uveitis. Ocul Immunol Inflamm 30, 652–663. https://doi.org/10.1080/09273948.2022.2032197.

Qu, Y., Zhao, C., Pei, M., Liang, A., Gao, F., Zhang, M., 2022. Anterior segment inflammation in pediatric uveitis is associated with reduced retinal vascular density as quantified by optical coherence tomography angiography. Ocul Immunol Inflamm 30, 392–396. https://doi.org/10.1080/09273948.2020.1803923.

Rao, N.A., Saraswathy, S., Wu, G.S., Katselis, G.S., Wawrousek, E.F., Bhat, S., 2008. Elevated retina-specific expression of the small heat shock protein, alphaA-crystallin, is associated with photoreceptor protection in experimental uveitis. Invest Ophthalmol vis Sci 49, 1161–1171. https://doi.org/10.1167/iovs.07-1259.

Reddy, A.K., Cabrera, M., Yeh, S., Davis, J.L., Albini, T.A., 2014. Optical coherence tomography-guided ranibizumab injection for cystoid macular edema in well-controlled uveitis: twelve-month outcomes. Retina 34, 2431–2438. https://doi.org/10.1097/IAE.0000000000000274.

Rong, J., Haider, A., Jeppesen, T.E., Josephson, L., Liang, S.H., 2023. Radiochemistry for positron emission tomography. Nat Commun 14, 3257. https://doi.org/10.1038/s41467-023-36377-4.

Rosenbaum, J.T., Woods, A., Kezic, J., Planck, S.R., Rosenzweig, H.L., 2011. Contrasting ocular effects of local versus systemic endotoxin. Invest Ophthalmol vis Sci 52, 6472–6477. https://doi.org/10.1167/iovs.11-7742.

Shevchenko, A., Wilm, M., Vorm, O., Jensen, O.N., Podtelejnikov, A.V., Neubauer, G., Shevchenko, A., Mortensen, P., Mann, M., 1996. A strategy for identifying gel-separated proteins in sequence databases by MS alone. Biochem Soc Trans 24, 893–896. https://doi.org/10.1042/bst0240893.

Sivanich, M.K., Gu, T.-J., Tabang, D.N., Li, L., 2022. Recent advances in isobaric labeling and applications in quantitative proteomics. Proteomics 22, e2100256. https://doi.org/10.1002/pmic.202100256.

Sole, M.J.D., Sande, P.H., Felipe, A.E., Fernandez, D.C., Sarmiento, M.I.K., Aba, M.A., Rosenstein, R.E., 2008. Characterization of uveitis induced by use of a single intravitreal injection of bacterial lipopolysaccharide in cats. Am. J. Vet. Res. 69, 1487–1495. https://doi.org/10.2460/ajvr.69.11.1487.

Tsirouki, T., Dastiridou, A., Symeonidis, C., Tounakaki, O., Brazitikou, I., Kalogeropoulos, C., Androudi, S., 2018. A focus on the epidemiology of uveitis. Ocul. Immunol. Inflamm. 26, 2–16. https://doi.org/10.1080/09273948.2016.1196713.

Venkateswaran, N., Galor, A., Wang, J., Karp, C.L., 2018. Optical coherence tomography for ocular surface and corneal diseases: a review. Eye and Vision 5, 13. https://doi.org/10.1186/s40662-018-0107-0.

Wang, L., Zhang, L., Wang, Z.-F., Huang, Z.-X., Hu, X., Gong, L., Tang, X., Liu, F., Luo, Z., Ji, W., Hu, W.-F., Woodward, Z., Zhu, J., Liu, Y.-Z., Nguyen, Q.D., Li, D.-W.-C., 2015. The role of αA-crystallin in experimental autoimmune uveitis. Curr Mol Med 15, 558–564. https://doi.org/10.2174/1566524015666150731101146.

Wang, L., Guo, Z., Zheng, Y., Li, Q., Yuan, X., Hua, X., 2021. Analysis of the clinical diagnosis and treatment of uveitis. Ann Palliat Med 10, 12782–12788. https://doi.org/10.21037/apm-21-3549.

Wang, X., Lou, N., Eberhardt, A., Yang, Y., Kusk, P., Xu, Q., Förstera, B., Peng, S., Shi, M., Ladrón-de-Guevara, A., Delle, C., Sigurdsson, B., Xavier, A.L.R., Ertürk, A., Libby, R. T., Chen, L., Thrane, A.S., Nedergaard, M., 2020. An ocular glymphatic clearance system removes β-amyloid from the rodent eye. Sci Transl Med 12, eaaw3210. https://doi.org/10.1126/scitranslmed.aaw3210.

William, R., Burch, R., 1960. The principles of humane experimental technique. Med. J. Aust. 1, 500. https://doi.org/10.5694/j.1326-5377.1960.tb73127.x.

Xu, B.Y., Mai, D.D., Penteado, R.C., Saunders, L., Weinreb, R.N., 2017. Reproducibility and agreement of anterior segment parameter measurements obtained using the CASIA2 and spectralis OCT2 optical coherence tomography devices. J Glaucoma 26, 974–979. https://doi.org/10.1097/IJG.0000000000000788.

Yadav, U.C.S., Ramana, K.V., 2019. Endotoxin-induced uveitis in rodents. Methods Mol Biol 1960, 161–168. https://doi.org/10.1007/978-1-4939-9167-9_14.

Zhang, J., Wu, J., Lu, D., To, C.-H., Lam, T.C., Lin, B., 2022. Retinal proteomic analysis in a mouse model of endotoxin-induced uveitis using data-independent acquisition-based mass spectrometry. Int J Mol Sci 23, 6464. https://doi.org/10.3390/ijms23126464.